Chapter 1
The K_2NiF_4-Type Cuprate Superconductors $La_{2-x}M_xCuO_4$ (M=Ba, Sr, Ca)

Fang Zhou

Abstract The K_2NiF_4-type compounds $La_{2-x}M_xCuO_4$ (M=Ba, Sr, Ca) are the cuprate superconductors which play an important role to the study of the intrinsic electronic properties and the influence of doping on superconductivity. Large and high-quality $La_{2-x}M_xCuO_4$ single crystals can be grown by TSFZ technique. The compounds are of a layered structure containing single CuO_2 planes and show remarkable and informative hole-doping dependent anomalies. In this chapter, the growth technique, including its up-to-date developments, and the detailed growth procedures are introduced. The doping effects on the superconductivity in $La_{2-x}Ba_xCuO_4$ and $La_{2-x}Sr_xCuO_4$, especially at certain specific magic hole concentrations, are presented.

1.1 Introduction

The discovery of superconductivity at $\sim$30 K in La–Ba–Cu–O system by Bednorz and Müller in 1986 [1] marks the beginning of the era of high-temperature cuprate superconductors. This superconducting system is derived from the parent compound La_2CuO_4, which, however, is an antiferromagnetic Mott insulator. La_2CuO_4 has a K_2NiF_4-type structure consisting of a stacking of single CuO_2 planes alternating with two LaO layers along *c* axis (Fig. 1.1a). The CuO_2 planes extending in *a*- and *b*-direction are the key structural unit common to all the cuprate superconductors discovered to date, which becomes superconducting as charge carriers of certain concentrations are doped into. The layer-structured cuprates are quasi-two-dimensional and the interplanar couplings of CuO_2 planes in the transverse *c*-direction are weak. Charge carriers of holes can be induced in the CuO_2 planes of La_2CuO_4 by partially substituting the trivalent rare-earth cations La^{3+} with, for instance, divalent alkaline-earth ones M^{2+} ($La_{2-x}M_xCuO_4$, M=Ba, Sr, Ca), or by intercalating oxygen anions to the interstitial sites in lanthanum tetrahedrons

F. Zhou (✉)
Institute of Physics, Chinese Academy of Sciences,
University of Chinese Academy of Sciences, 100190 & 100049 Beijing, China
e-mail: fzhou@iphy.ac.cn

D. Chen et al., *Growth and Characterization of Bulk Superconductor Material*,
Springer Series in Materials Science 243, DOI 10.1007/978-3-319-31548-5_1

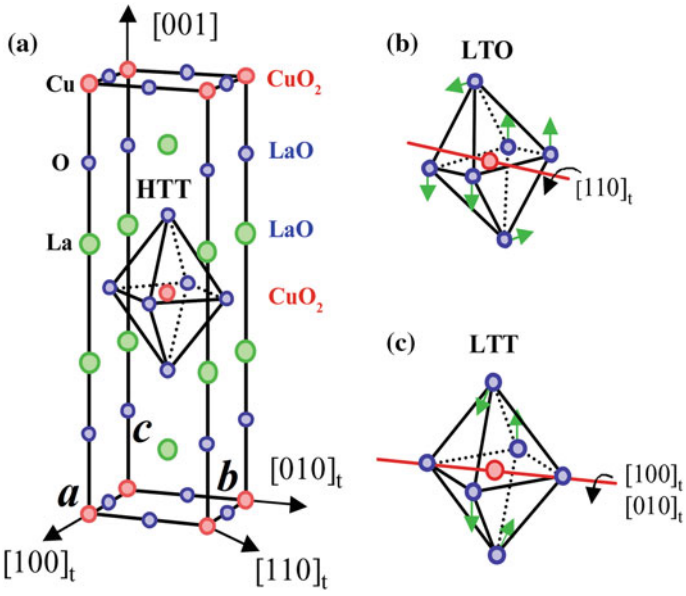

Fig. 1.1 **a** Unit cell of La_2CuO_4 in the HTT phase (*I4/mmm*). **b** Tilt direction of the CuO_6 octahedra in the LTO phase (*Bmab*). **c** The CuO_6 octahedra in the LTT phase ($P4_2/ncm$) tilt alternatively about $[100]_t$ and $[010]_t$ in adjacent layers. From [2]

via electrochemical oxidation [3, 4] and/or under high oxygen pressures ($La_2CuO_{4+\delta}$) [5, 6]. In this chapter, the cations doped $La_{2-x}M_xCuO_4$ are concerned, where the insulating (La^{3+}, M^{2+})O layers serve as the charge "reservoir".

The parent state of CuO_2 planes in undoped La_2CuO_4 is schematically represented in Fig. 1.2 [7]. The Cu/O atoms form an approximately square lattice, with a

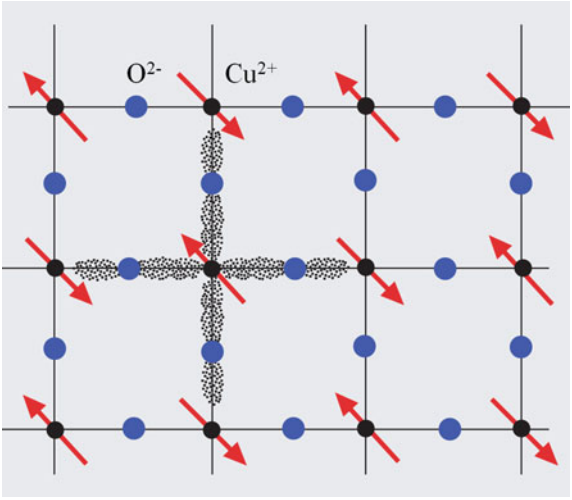

Fig. 1.2 The undoped state of CuO_2 plane formed by Cu–O–Cu square lattice. From [7]

Cu–O–Cu spacing ~3.8 Å for the nearest-neighboring Cu's bonded to "p_σ orbitals" (the shaded area) of the O atoms in between them. The highest occupied band contains one electron per unit cell, which cannot move owing to strong electron-electron repulsion at a doubly occupied site supposed to be created by its jumping. The Mott insulator differs fundamentally from a conventional band insulator, where electron motion is blocked by the Pauli exclusion principle when the highest occupied band contains two electrons. The superexchange interaction mediated by the oxygen "p_σ orbitals" favors anti-parallel spin alignment on the nearest-neighboring Cu sites as indicated by the red arrows, leading to the long-range antiferromagnetic order. Upon the electron occupancy per unit cell is reduced from 1 to $1-x$ by doped holes of a concentration x, the antiferromagnetic ordering temperature decreases rapidly (schematic red region in Fig. 1.3), and charge conduction is restored as the hole doping creates sites to which electrons can jump without suffering the Coulomb repulsion. When doped with sufficient amount of holes, the superconducting long-range order occurs in a dome-like blue region in Fig. 1.3. The doping level at which the superconducting transition temperature (T_c) is maximal is referred to as "optimal", while those lower and higher than the optimal one as "under-doping" and "over-doping", respectively.

The high-temperature tetragonal (HTT) structure of La_2CuO_4 with the *I4/mmm* symmetry is characteristic of untilted CuO_6 octahedra thus ideally flat CuO_2 planes (Fig. 1.1a). With decreasing temperature, La_2CuO_4 undergoes a second-order transition at 525 K [8] from the HTT phase to a low-temperature orthorhombic (LTO) phase of the space group *Bmab*. The CuO_6 octahedra of LTO structure are tilted by a small angle about the tetragonal $[110]_t$ axis (Fig. 1.1b), so that the CuO_2 planes become to be buckled to certain extent rather than flat. The LTO unit cell is doubled, with its orthorhombic $[100]_o$ axis along the tilt axis diagonal to the Cu–O–Cu square lattice shown in Fig. 1.2. In Ba doped $La_{2-x}Ba_xCuO_4$ (LBCO) system, in addition, occurs at lower temperatures a first-order transition from LTO to another

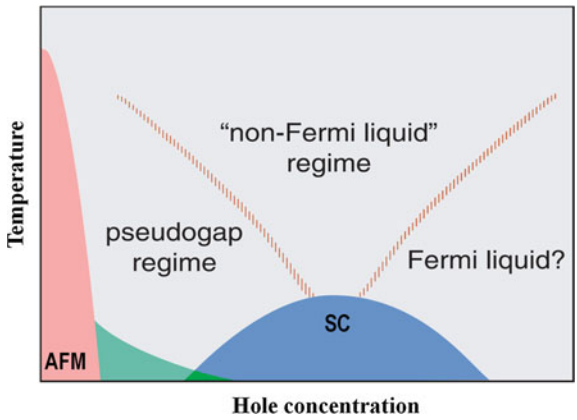

Fig. 1.3 Schematic of electronic phase diagram for hole-doped cuprate superconductors. From [7]

low-temperature phase of either a low-temperature tetragonal (LTT; *S.G.* $P4_2/ncm$) or a low-temperature less-orthorhombic (LTLO; *S.G. Pccn*) structure [2]. In LTT phase, the CuO_6 octahedra tilt about the axis parallel to the square lattice, but alternatively along $[100]_t$ and $[010]_t$ directions in adjacent octahedron layers (Fig. 1.1c) [9–11]. In LTLO the tilt axis runs along an intermediate in-plane direction [12]. In LBCO, doping dependent static stripe order correlated with the LTO-LTT structure transition strongly suppresses the superconductivity; while in Sr doped $La_{2-x}Sr_xCuO_4$ (LSCO) where the LTT phase is absent, instead robust intrinsic superconducting states emerge in the vicinity of some specific *magic* hole concentrations.

High-quality single crystals are requisite to the study on intrinsic physical properties of high-T_c cuprate superconductors. Anisotropic electronic properties of the cuprates, quasi-two-dimensional in crystal and electronic structures, can be measured reliably only on single crystal samples, and the samples of large size are demanded by important measurements such as, especially, neutron scattering. Compared to crystal growth from a flux solution by slow cooling or top-seeding, the travelling-solvent floating-zone (TSFZ) technique has proven to be the only one capable of fabricating ten-centimeter long high-quality K_2NiF_4-type and other cuprate single crystals of pure phases with uniform and controllable doping levels. It is also very successful in growing large binary FeSe superconductor [13] and many other functional materials [14].

In Sects. 1.2, 1.3 and 1.4, we will focus on concept, technique and experiment aspects with regard to TSFZ procedures. The doping effect on the superconductivity of LBCO and LSCO, especially at certain particular magic hole-doping fractions, will be presented in Sect. 1.5. We will conclude in Sect. 1.6 with general remarks.

1.2 Phase Diagram and Distribution Coefficient of Dopants in La_2CuO_4

The stoichiometric compound La_2CuO_4, formed in pseudo-binary La_2O_3–CuO system, melts incongruently at a peritectic temperature ~1327 °C (Fig. 1.4) [15]. Below this temperature, the composition of liquid in equilibrium with La_2CuO_4 of 50 mol% CuO ranges approximately from 75 to 90 mol% CuO in the temperature range from ~1327 to ~1075 °C, following the liquidus line. These are the composition and temperature conditions feasible to grow incongruent La_2CuO_4 from the liquid. In a corresponding solid-liquid equilibrium available for a solid-solution system, the solubility of a dopant in the solid-solution phase (x_S) differs from its solubility in the liquid phase (x_L). The ratio of the two given concentrations, dependent on each other, is defined as the distribution coefficient $k = x_S/x_L$. For non-stoichiometric $La_{2-x}M_xCuO_4$ as an M doped solid-solution, the effective distribution coefficients k_{eff} for Ba, Sr and Ca dopants in a slow-cooling

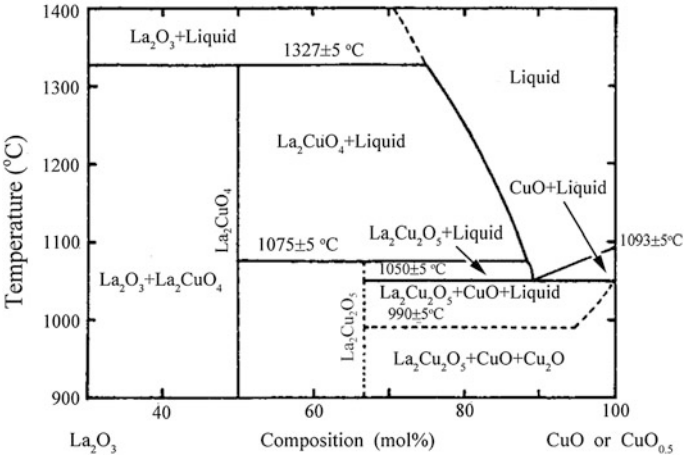

Fig. 1.4 Phase diagram of La_2O_3–CuO system in oxygen. From [15]

floating-zone (SCFZ) process [16] were determined earlier [17, 18]. The results at different doping levels are shown in Fig. 1.5. That can be taken as a starting point for one to estimate the optimal dopant contents in the solvents from which $La_{2-x}M_xCuO_4$ can be crystallized in a travelling-solvent floating-zone process.

Figure 1.6a is a schematic phase diagram for a hypothetical binary A–B system with solid-solution regions including β. The β phase exists below a peritectic temperature T_p within a certain range of composition, no longer forming a "line phase", like La_2CuO_4, at a specific peritectic composition P. The solid-solution β at S of a composition x_S is in equilibrium with the liquid at L (the solvent) of a composition x_L different from x_S. The distribution coefficient is less than unity as $x_S < x_L$, the same as those for $La_{2-x}M_xCuO_4$. In a thermodynamic equilibrium process, any shift of solvent L on the liquidus line (as indicated by the red arrows) resulting from a

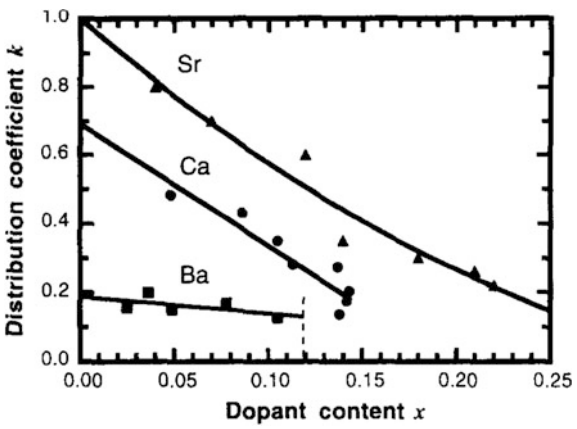

Fig. 1.5 Effective distribution coefficients of the dopants Sr, Ca and Ba into La_2CuO_4. From [18]

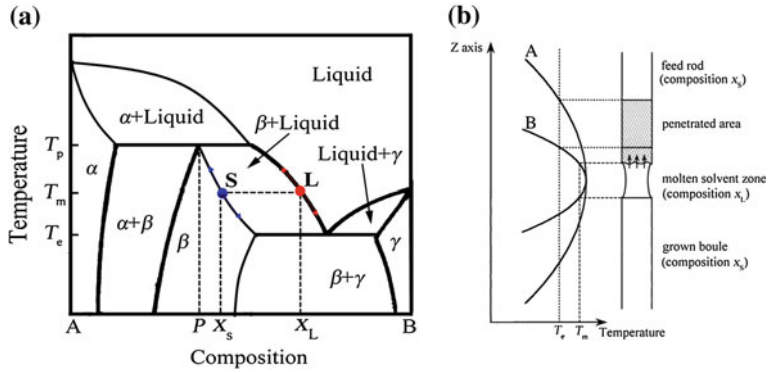

Fig. 1.6 **a**. Phase diagram for a hypothetical binary A–B system with solid-solution regions including β. **b** (Adapted based on Fig. 10 of [19]). Schematic illustrations of a TSFZ configuration for the solid-solution β at S of the composition x_S in equilibrium with the solvent L of the composition x_L, as the case shown in (**a**), and of the solvent penetration reduced by a sharper vertical temperature profile B. Here T_m and T_e are the melting (or dissolving) and eutectic temperatures, respectively, as indicated in (**a**)

variation in composition and/or temperature will lead to a corresponding shift of solid S on the solidus line (indicated by the blue arrows), i.e., the composition of solid-solution S will change concomitantly. That is what should be prevented if one wants to grow a doped incongruent compound with a fixed composition x_S throughout the sample. Experimentally, it depends on how to control a constant composition and temperature of the solvent from which the crystal is being grown.

1.3 Travelling-Solvent Floating-Zone (TSFZ) Technique

The TSFZ technique was first reported in the crystal growth of incongruent compounds of yttrium iron garnet (YIG, $Y_3Fe_5O_{12}$) with the pure [20] or substituted [21] compositions, after a successful attempt to grow incongruent YFe_2O_4 [22]. Thanks to its unique vertical configuration (Figs. 1.6b and 1.7), this technique is specially suited for growing doped incongruent materials from melts. The vertical design makes it possible for a molten solvent zone of an average composition x_L to form in between an as-grown crystal of a composition x_S and a feed rod of almost the same composition as the crystal (Fig. 1.6a, b). In a stable TSFZ process, at both the growth and melting (or dissolving) interfaces, the solid phase S, with the composition x_S and at the temperature T_m, is in a quasi-thermodynamic equilibrium with the molten solvent phase L, composition x_L and temperature T_m, corresponding to the solid-liquid equilibrium between S and L shown in Fig. 1.6a. This is the basic thermodynamic condition required for a smooth and successful TSFZ growth process. The molten solvent is held in position by its surface tension when travelling upwards. A usual focused infrared-heating establishes at the growth and melting

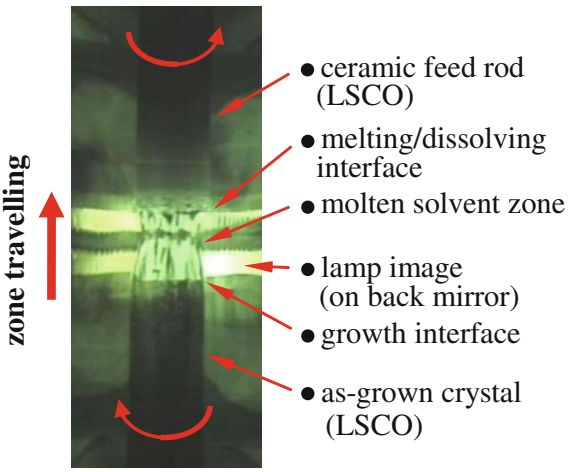

Fig. 1.7 A snapshot in a smooth and successful TSFZ growth process of a $La_{2-x}Sr_xCuO_4$ single crystal

interfaces a high vertical temperature gradient, like the case of temperature profile B in Fig. 1.6b, which is the driving force for crystal growth. The crucible- and flux-free growth, void of contamination from container materials and other impurities, is carried out in a space enclosed by a quartz tube. In the following we will take actual cases as example to discuss the essentials involved in TSFZ procedures.

A typical smooth and successful growth process of a $La_{2-x}Sr_xCuO_4$ single crystal [23, 24] is shown in Fig. 1.7. It is characteristic of a very stable molten zone with well-defined solid-liquid borders. The molten zone was heated at a constant power by four halogen lamp-images focused with a horizontal quartet ellipsoidal mirror (not shown). The almost isodiametric cylindrical feed rod was made of well-prepared polycrystalline $La_{2-x}Sr_xCuO_4$, with a small CuO excess to compensate for its evaporation during the growth. A ceramic solvent pellet was prepared separately, with an initial composition rich in CuO (78–84 mol% CuO) based on the phase diagram (Fig. 1.4) and an appropriate content of Sr estimated by taking into account its effective distribution coefficients k_{eff} (Fig. 1.5). The solvent pellet was heated to melt between the feed rod and a seed crystal in the very beginning. The feed rod and grown crystal were rotated in opposite directions to improve liquid homogeneity and to achieve uniform horizontal temperature profiles encircling the molten zone.

As the molten zone slowly travels upwards at a constant rate with a mechanical motion of the heating parts, at the lower growth interface, $La_{2-x}Sr_xCuO_4$ crystal is continuously precipitated from the molten solvent in equilibrium with it, while simultaneously at the upper melting interface, an equal amount of polycrystalline $La_{2-x}Sr_xCuO_4$ is dissolved from the feed rod into the molten solvent to compensate for the mass consumption including the evaporation loss of CuO. Therefore a slow growth (travelling) rate and a well-stirring by the rotation are required to allow for a sufficient mass transportation in the molten zone. A dense, isodiametric and straight

feed rod is important for keeping a stable shape and volume of the molten zone, in which case a constant temperature distribution in the molten zone is expected at a fixed heating power, provided a small variation in the ambient temperature. With proper manipulations, such a self-stabilizing growth process, like that shown in Fig. 1.7, can be maintained, usually starting from a growth length about one centimeter, more or less. As a consequence, both the composition and temperature distributions of the molten solvent zone will be kept constant. From this point onward until the end of growth, the duration about one week, uniformly doped high-quality large single crystal of the exact chemical formula $La_{2-x}Sr_xCuO_4$ can be continuously grown from the solvent.

However, an unstable molten zone does happen in some cases, sometimes depending on materials. If the feed rod is less dense and uniform, the solvent may severely penetrate into the feed rod through capillary intertices until reaching a eutectic point at T_e (shaded area in Fig. 1.6b). In a worse case, that may lead to a harmful jagged melting interface with varying shapes, causing fluctuations in the volume (shape), composition and temperature of the molten zone. Experimentally, that may be avoided or reduced to a great extent with a well-prepared highly dense feed rod [23–25], or by improving the vertical temperature gradient (Fig. 1.6b) [19, 26], or by adding a certain amount of B_2O_3 into the solvent in its preparation process [27]. Moreover, a steep temperature gradient will also prevent some possible unstable growth interface from happening. For instance, an unstable growth interface would otherwise develop in presence of a constitutional supercooling related to a rejection of excess CuO and Sr into liquid during crystallization, because of the distribution coefficients <1. Besides, while an approximately flat growth interface is ideal for crystal growth, the real growth, and melting as well, interfaces become convex into molten zone and more as closer to the centers. Occasionally the two interfaces even touch one another. A fast rotation is usually needed to reduce the interface convexity.

1.4 TSFZ Growth and Characterization of $La_{2-x}M_xCuO_4$

The earliest attempts to grow the K_2NiF_4-type cuprate crystals by slow cooling or top-seeding flux methods date back to the year of 1987, soon after the Bednorz and Müller's paper. Among them, superconducting LSCO crystals up to 8 mm in lateral dimension was grown from CuO flux solution [28]. The TSFZ technique was first applied in growing larger LSCO single crystals in 1989, and an as-grown crystal ~6 mm in diameter and 40 mm in length was obtained [29, 30]. Since then, much work has been done in the TSFZ growth and characterization of $La_{2-x}M_xCuO_4$ crystals, especially the $La_{2-x}Sr_xCuO_4$ system exhibiting a wide doping range for Sr atoms. This section will not aim to be systematically documented, but will rather pay attention to subsequent improvements and developments in this field.

Precursor powders for $La_{2-x}M_xCuO_4$ feed rods were commonly prepared by solid-state reactions using as raw materials relevant high-purity oxides and

alkaline-earth carbonates or nitrates [25]. A small amount of CuO (1–4 mol%) in excess was added in order to compensate for its evaporation loss. The precursor powders were hydrostatically pressed under a high pressure of hundreds MPa to form a compact cylindrical rod, before it was well-sintered and post-processed into a ceramic feed rod good for TSFZ growth.

As emphasized earlier, fabrication of a dense and uniform, in both composition and heating history, feed rod is an important step in TSFZ procedures. The precursor powders very fine in particle size and homogeneous in composition would have a high sintering activity. Highly fine and micro-homogeneous precursor powders were produced via sol-gel approaches [24, 25], and, combined with a hydrostatic pressing under a high pressure over 600 MPa, very dense and uniform LSCO feed rods were obtain after *well-sintered* at elevated temperatures of 1240–1280 °C, depending on compositions, for a short duration of 2 h [24]. That contributed much to a smooth and stable TSFZ growth. Special attention should be paid to make a uniformly sintered feed rod usually over dozen-centimeter long. It proves that a kind of vertical furnace is effective for the purpose, where, during sintering, the feed rod can be kept rotating and moving up and down to attain an identical heating history throughout the whole rod.

The solvent pellets were prepared by the solid-state reaction in a simpler way. The composition was rich in CuO (77–85 mol% CuO), based on the phase diagram of La_2O_3–CuO (Fig. 1.4). The concentration of dopant M in solvent was appropriately chosen considering the distribution coefficients (Fig. 1.5), so that the proper solid-liquid equilibrium could be established through self-adjusting of the TSFZ process soon after the start of crystal growth. In order to reduce bubbles possibly emerging in molten solvent at the very start, it was suggested to heat the pellets at a high enough temperature just below the melting temperature [24].

The use of seed crystals along tetragonal $[100]_t$ or $[110]_t$ directions is effective to achieve a well oriented TSFZ growth, though the growth can also be started on a polycrystalline rod as a "pseudo-seeding" [25]. The crystal growth was usually carried out under 0.2–0.4 MPa oxygen pressure. A common growth rate was 1 mm/h, while slower rates of 0.4–0.8 mm/h were also used in some experiments. Some experimental details involved in TSFZ procedures were also discussed in the literature [14, 31–36].

A series of under- and over-doped LSCO single crystals of high quality were grown by TSFZ [18, 23, 36], showing a crystal mosaicity of 0.10° in terms of the full-width-at-half-maximum (FWHM) of x-ray rocking curves for (006) [36] or (008) [23] Bragg reflections. A typical large-sized as-grown $La_{2-x}Sr_xCuO_4$ ($x = 0.11$) crystal, ~6.6 mm in diameter and 100 mm in length, is shown in Fig. 1.8, which has been carefully checked to be subgrain-free after a distance of growth (usually 2–3 cm) starting on a seed crystal [23, 24]. Thanks to the use of highly dense and uniform feed rods and a slow growth rate of 0.6 mm/h, large $La_{2-x}Sr_xCuO_4$ single crystals of higher quality were produced [24]. Double-crystal x-ray rocking curves of (008) reflection show the much smaller crystal mosaic of only 113–150 arcsec. (0.03–0.04°) in terms of FWHM (Fig. 1.9a); and the x-ray Laüe spots from different crystal orientations are all well defined and can be well

Fig. 1.8 Photograph of an as-grown $La_{2-x}Sr_xCuO_4$ ($x = 0.11$) crystal ~6.6 mm in diameter and 100 mm in length. From [24]

indexed, as evident in the Laüe patterns for (001) (Fig. 1.9b), $(100)_t$ (Fig. 1.9c) and $(110)_t$ (Fig. 1.9d) crystal planes in tetragonal notation.

In the over-doping regime of $La_{2-x}Sr_xCuO_4$, however, subgrains were present for $x = 0.25$ and 0.30 crystals grown at a rate of 1.0 mm/h, as well as inclusions of $La_{2-x}Sr_{1+x}Cu_2O_{6+\delta}$ for $x = 0.30$ besides the subgrains [18]. Formation of the

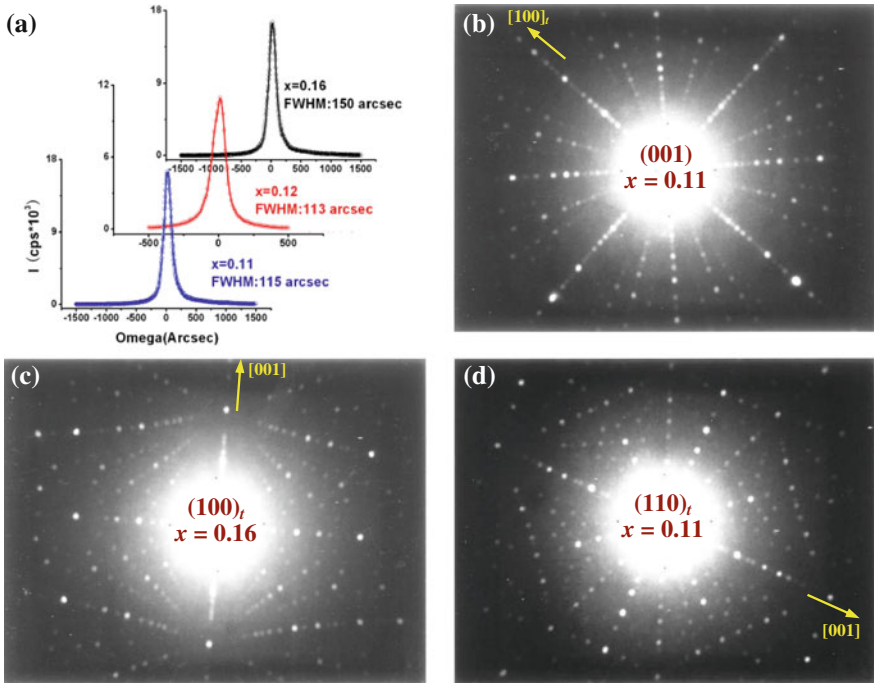

Fig. 1.9 **a** Double-crystal x-ray rocking curves of (008) Bragg reflection for $La_{2-x}Sr_xCuO_4$ ($x = 0.11$, 0.12, 0.16) single crystals grown by TSFZ. **b–d** are the x-ray back-reflection Laüe patterns with different crystal orientations along (001) (for $x = 0.11$), $(100)_t$ (for $x = 0.16$) and $(110)_t$ (for $x = 0.11$) planes in tetragonal notation, respectively. **a** and **b** are from [24]; **c** and **d** are reported for the first time here

subgrains could be avoided at a slower rate of 0.8 mm/h. The precipitation of $La_{2-x}Sr_{1+x}Cu_2O_{6+\delta}$ was attributed to a constitutional supercooling related to a high Sr content in the solvent.

An under-doped $La_{2-x}Sr_xCuO_4$ ($x = 0.08$) crystal was specially grown using a double lamp-image furnace, as this doping level is close to 0.09 at which HTT-LTO transition occurs at room temperature [25]. The sample of $T_c \sim 20$ K displayed, as expected, a weak orthorhombicity compared to parent La_2CuO_4. The rocking curve of neutron diffraction gave a FWHM $\sim 0.2°$ for (006) reflection.

A series of highly under-doped $La_{2-x}Sr_xCuO_4$ single crystals, spanning the insulating-superconducting phase boundary, were grown by TSFZ method [37]. The onset superconducting transition temperatures were observed to be 6.3, 11.6, and 17.0 K for the samples with $x = 0.056$, 0.06, and 0.07, respectively. No superconductivity was detected for $x = 0.053$ down to 2 K. The lower critical concentration x_c for superconductivity was thus estimated to lie between $x = 0.053$ and 0.056.

$La_{2-x}Ba_xCuO_4$ crystals of $x < 0.15$ were grown by TSFZ using crystallized feed rods under low oxygen partial pressures (10^{-2}–10^{-3} atm), in order to reduce an otherwise deep penetration of solvent into feed rod and a formation of Ba-enriched compounds resulting in molten zone instability [33]. The growth rate was slow (0.5 mm/h) to avoid impurity phases in the crystals and a La_2CuO_4 crystal was used as the seed. The typical size of grown boules was 4 mm in diameter and 100 mm in length, but a mosaic structure was present in the crystals by Laüe experiment. The crystals doped at $x \sim 0.10$ and 0.14 showed onset superconducting transitions at 23 and 25 K, respectively. However, higher O_2 pressures (0.2–0.4 MPa) were also used to grow $La_{2-x}Ba_xCuO_4$ crystals by TSFZ [38, 39]. Under 0.4 MPa pressure of flowing O_2, $La_{2-x}Ba_xCuO_4$ ($x = 0.11$) single crystal of good quality was grown at a rate of 1.0 mm/h [39]. The feed rod was in 1 mol% excess of CuO; the solvent composition was of a molar ratio $(La_{1.875}Ba_{0.125})$:Cu = 3:7, corresponding to 82 mol% CuO in La_2O_3–CuO phase relation. La_2O_3 inclusions were observed in initially grown part of the as-grown ingot, which broke into pieces a few days in air. A single crystal 5 mm diametral and 20 mm long was obtained from the rest part, showing a depressed $T_c \sim 10$ K as expected because of this doping level (0.11) close to that of "1/8 anomaly". Two kinks at ~ 256 and ~ 53 K evident in the temperature dependences of electrical resistivity were attributed to HTT-LTO and LTO-LTT structural transitions, respectively. Strongly suppressed T_c's of 4 K or ~ 2.4 K were reported for exact $x = 1/8$ LBCO single crystals grown by TSFZ [40, 41].

The solubility limit of Ca in La_2CuO_4 was determined to be about 0.14 in a SCFZ process [17]. However, the doping level of Ca in $La_{2-x}Ca_xCuO_4$ crystals grown by TSFZ seemed to be saturated at $x \sim 0.10$, despite its further increased concentrations in feeds and solvents [18, 42]. The as-grown ingot was of a 5 mm diameter and a 30 mm length. The grown crystals of $x = 0.05$ did not superconduct down to 5 K. The superconductivity in the crystals of $x = 0.075$ and 0.09 was observed to occur at $T_c \sim 15$ K, independent on the Ca concentration, and to show a broadened and unsaturated diamagnetic transition.

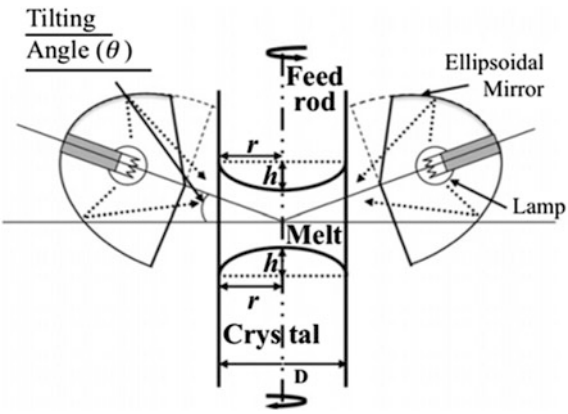

Fig. 1.10 Schematic drawing of the tilting-mirror image furnace. From [43]

By the horizontally designed common lamp-image heating, the diameter of grown crystal is limited owing to the interface convexity. It was reported that, using a quartet ellipsoidal mirror tilted up by an angle θ (Fig. 1.10), LSCO crystals of a larger diameter could be grown [43]. At a tilting-angle $\theta = 20°$, this kind of TSFZ experiment yielded LSCO crystals with a maximum diameter of 10 mm. The experimental results suggested that the evaporation of CuO was reduced with increasing tilting-angle. At the same time, however, the vertical temperature gradient at the melting interface was also reduced.

Recently, an important development in TSFZ technique is the use of laser diodes as the heating source: five or seven laser diodes assembled surrounding the molten zone produce parallel and homogeneous well-concentrated laser beams of a wavelength 975 nm and a rectangular cross section [44]. By this laser-heating, the average vertical temperature gradient can be substantially increased, ~5 times higher than the lamp-image heating, and a more uniform horizontal temperature distribution encircling the molten zone be attained as well. The laser-heating enables stable and reproducible crystal growth of some incongruently melting materials difficult to be grown by conventional techniques, for example the materials of LBCO and $BiFeO_3$ [45].

1.5 Doping Effect on Superconductivity: 1/8 Anomaly in $La_{2-x}Ba_xCuO_4$ and Magic Doping Concentrations in $La_{2-x}Sr_xCuO_4$

Intensive studies have been made on the preparation of both the poly- and single-crystal samples of $La_{2-x}M_xCuO_4$, and their physical properties characterized by various probes including, for instance, transport and magnetic measurements, neutron scattering and ARPES. Among the hole-doped cuprates, $La_{2-x}Sr_xCuO_4$ (LSCO) tolerates the dopant (Sr) in a wide range of concentration, leading to a more complete electronic phase diagram. At a very low doping ($x < 0.02$), LSCO is an

antiferromagnetic Mott insulator. After crossing a spin-glass state ($0.02 < x < 0.05$, the schematic green region in Fig. 1.3) [46, 47], it becomes a superconductor ($0.05 < x < 0.26$) and then behaves as a normal metal ($0.26 < x < 0.6$) [48] before finally turns out to be a semiconductor ($x > 0.6$) [49]. In the superconducting regime, the critical temperature of LSCO reaches its maximum (38 K) at the hole density $x = 0.16$.

The investigation on the doping and temperature dependences of physical properties is important for acquiring a better understanding of high-T_c superconductivity and strong electron correlation in cuprates. For example, although the superconducting critical temperature T_c of LSCO shows in general a dome-shaped doping dependence, a "plateau" at 30 K, like that shown in Fig. 1.11, always appears around the doping level $x = 1/9$ (~ 0.111) in the underdoping regime [50–53]. This is in contrast to the observation on $La_{2-x}Ba_xCuO_4$ (LBCO) where the superconductivity almost disappears at $x = 1/8$ (0.125), leading to a double T_c maximum (~ 30 K) at $x \sim 0.095$ and ~ 0.155 (Fig. 1.12). The "1/8 anomaly" in LBCO arousing much interest in the field of high-T_c cuprates has been clarified to correlate with one-dimensional static charge and spin stripe order, which coincide with and develop below, respectively, the structure transition from LTO to LTT phase [2]. The stripe order pinned by the electron-lattice coupling [54] is most pronounced at $x = 1/8$, where both diffraction peak intensities for charge and spin stripe order show a maximum while fall off for $x \neq 1/8$ (Fig. 1.13).

In $La_{2-x}Sr_xCuO_4$, however, the LTT phase is absent. Instead, two distinct intrinsic superconducting phases noticeably develop in the vicinity of specific

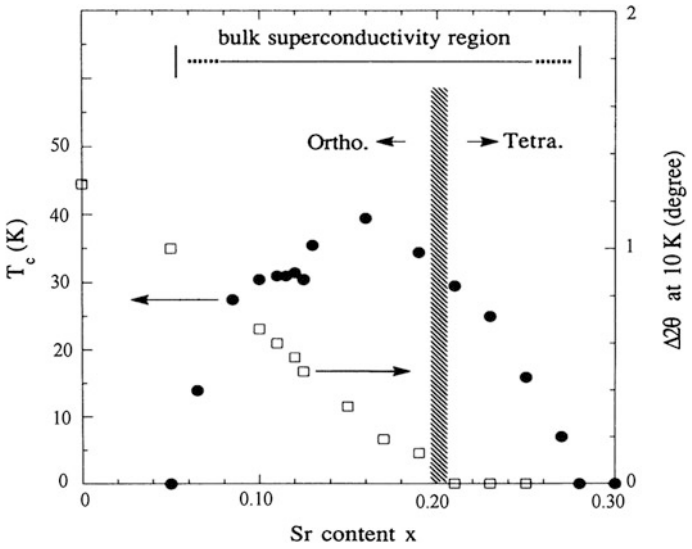

Fig. 1.11 Doping dependence of T_c (*solid circles*), the bulk superconductivity region and orthorhombic splitting (400)-(040) at 10 K (*squares*) in $La_{2-x}Sr_xCuO_4$. From [50]

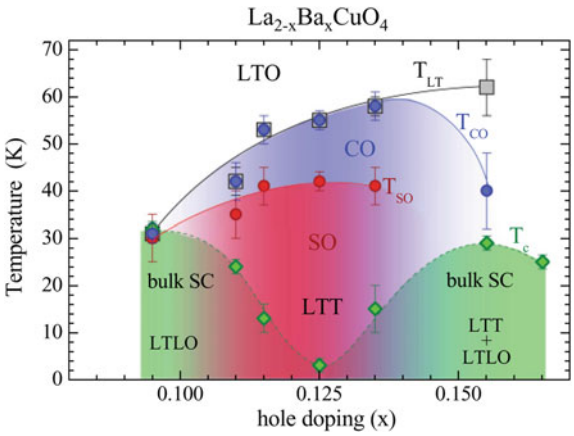

Fig. 1.12 Temperature vs hole-doping phase diagram of $La_{2-x}Ba_xCuO_4$ single crystals. Onset temperatures: T_c of bulk superconductivity (SC), T_{CO} of charge stripe order (CO), T_{SO} of spin stripe order (SO), and T_{LT} of the low-temperature structural phases LTT and LTLO. At base temperature CO, SO, and SC coexist at least in the crystals with $0.095 \leq x \leq 0.135$. *Solid* and *dashed lines* are guides to the eye. From [2]

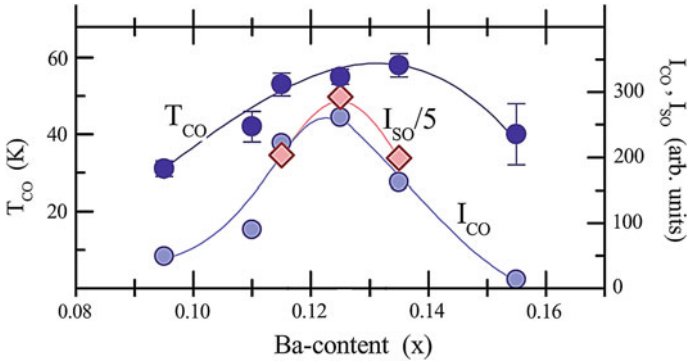

Fig. 1.13 Diffraction peak intensities I_{CO} and I_{SO} for charge and spin stripe order, respectively, and the charge stripe order temperature T_{CO} as functions of doping in $La_{2-x}Ba_xCuO_4$. From [2]

magic hole concentrations of $x = 1/4^2$ (0.0625) and $1/3^2$ ($\sim$0.111), respectively, in the under-doping regime. This has been evidenced by the studies of magnetism, far-infrared charge dynamics and electron transport on a series of high quality $La_{2-x}Sr_xCuO_4$ single crystal samples (x = 0.063, 0.070, 0.090, 0.100, 0.111, 0.125) [23, 52, 53, 55–57].

The so-called magic doping concentrations are two-dimensional hole densities $P_{MD} = m/n^2$ where m and n are positive integers with, for the two most prominent series, n = 3 or 4 and $m \leq n$ [58]. The intrinsic superconducting phases at the magic

dopings are characteristic of a single narrow diamagnetic transition with an onset T_c of either 15 K ($x = 1/4^2$) or 30 K ($x = 1/3^2$) which remains robust under fields up to 5 T, and of a local minimum ($x = 1/4^2$) or an unusual drop ($x = 1/3^2$) in the Meissner fraction (Fig. 1.14) [52, 57]. This is in sharp contrast to the apparent non-intrinsic superconducting phases at some other doping levels showing a much broader diamagnetic transition and a field-sensitive onset T_c which settles from a higher value into either 30 K or 15 K, depending on dopings, as the field increases above 1 T (see Fig. 3 of [57]). Such field dependences of T_c are characteristically different from that of conventional type II superconductors or granular superconductors where there is only one non-robust superconducting state showing a monotonic decrease in T_c under field.

Nevertheless, those apparently puzzling phenomena are explicable from the dynamic nano-scale domains of charge phases with a *universal* length scale (300–1100 Å) [59]. By systematically examining the field-dependent Meissner signal sizes in various crystal samples, in terms of the comparability of inter-vortex spacing to the universal length scale of underlying dynamic electronic textures, it has been argued that there is a distinct superconducting condensate state for each intrinsic superconducting phase, suggesting that the intrinsic superconducting phases at magic doping concentrations are the pristine electronic phases for high-T_c superconductivity [57]. The formation of the intrinsic superconducting states is

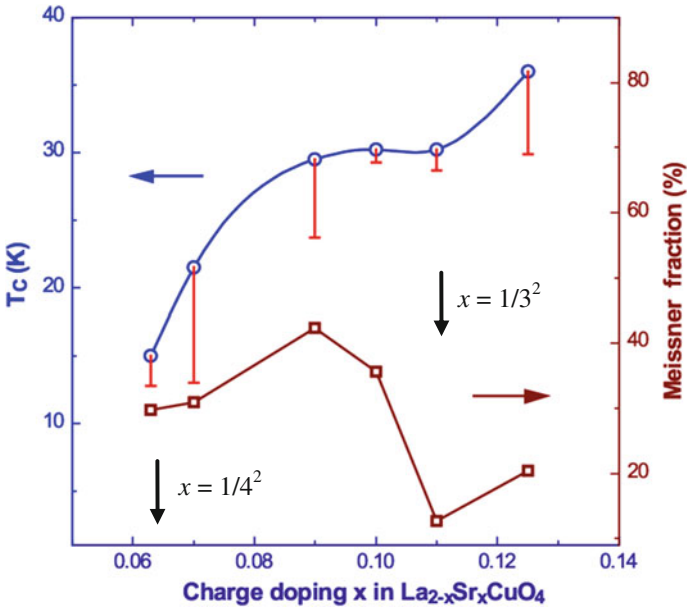

Fig. 1.14 Onset superconducting transition temperature T_c, transition width (indicated by the length of the *vertical bars*) and Meissner fraction as functions of hole concentration for $La_{2-x}Sr_xCuO_4$ single crystals ($x = 0.063$, 0.070, 0.090, 0.100, 0.111, 0.125). The data were obtained from dc magnetic measurements. Lines are guides to the eye. From [52]

compatible with a *composite* charge model [55]. This charge model stresses that only a very small fraction of the total holes, coupled to underlying *two-dimensional charge lattices* formed by the rest of the holes, is responsible for the superconductivity and the normal state free charge transport, including intrinsically coherent *c*-axis charge transport [56].

Moreover, at the magic hole density $x = 1/9$ ($n = 3$), a new phase boundary $T_{m2}(H)$ has recently been discovered below the first order vortex melting line in the vortex solid phase, by field-cooled magnetization measurements on $La_{1.89}Sr_{0.11}CuO_4$ single crystal and critical scaling analysis (Fig. 1.15) [58]. The coupling between superconductivity and antiferromagnetism has been found to be attractive below $T_{m2}(H)$ with a negative coupling constant $\nu < 0$, evidencing that the antiferromagnetism microscopically coexists and collaborates with the high-T_c superconductivity in cuprates.

At another magic doping $x = 1/16$ ($n = 4$), despite the extremely under-doping level in the vicinity of an insulator-superconductor transition, a remarkably sharp quasiparticle peak in the nodal region was observed in $La_{1.937}Sr_{0.063}CuO_4$ single crystal by high-resolution ARPES (Fig. 1.16a) [60]. The sharp peak abruptly turns into a broad edge upon energy dispersing above ~70 meV (indicated by a red arrow). Meanwhile, an enhanced upturn in the MDC (momentum distribution curve) width, proportionally related to the scattering rate of electrons, was evident at the same energy scale (Fig. 1.16b) [61], suggestive of a stronger scattering mechanism above ~70 meV.

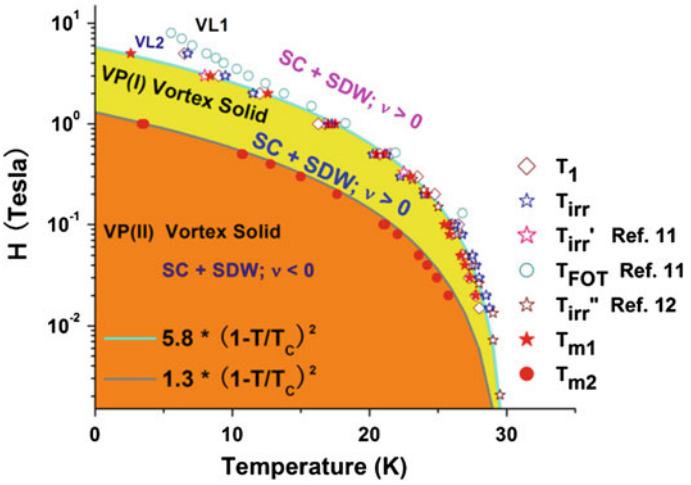

Fig. 1.15 Magnetic phase diagram of $La_{2-x}Sr_xCuO_4$ crystals around $x = 1/9$. Various characteristic temperatures identified by magnetic measurements (T_1 & T_{irr}), reported in the literatures (T'_{irr}, T''_{irr} & T_{FOT}) and extracted by the critical fittings (T_{m1} & T_{m2}) are plotted together for comparison. $T_{m1}(H)$ & $T_{m2}(H)$ are the boundaries separating vortex liquid (VL) phase from vortex phase I (VP(I)) and VP(I) from vortex phase II (VP(II)), respectively. From [58]

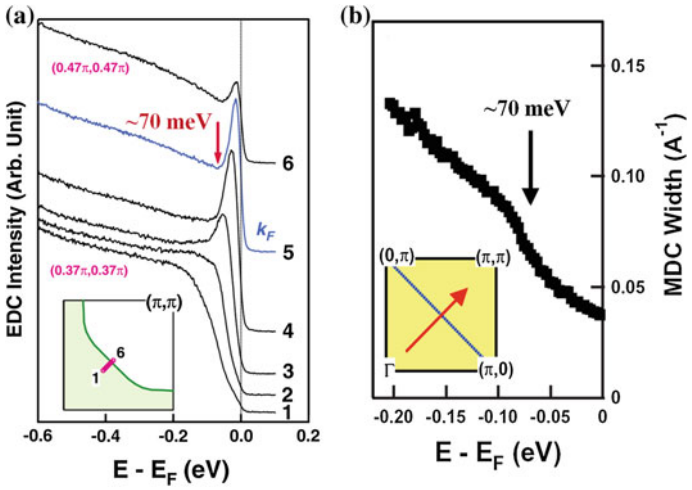

Fig. 1.16 Some ARPES data on $La_{1.937}Sr_{0.063}CuO_4$ ($x \sim 1/16$) single crystal at 20 K. **a** Energy distribution curves (EDCs) along the nodal direction in a second Brillouin zone. The *red arrow* indicates the energy of ~70 meV below which the quasiparticle survives and above which it turns into a broad edge. From [60]. **b** The MDC width (electron-scattering rate) shows an enhanced upturn at the same energy scale ~70 meV, as indicated by an arrow. From [61]

Recently, it has been shown that, in the under-doping regime, a maximum stabilization energy is gained at the magic number concentrations of $n = 4$ ($x = 1/16$) and 3 ($x = 1/9$) for two-dimensional lattices formed by holes of oxygen-character and b_{2g} symmetry [62]. Interestingly, a maximum energy gain arises as well at the hole density $x = 0.100$, which bears the same feature of a single narrow diamagnetic transition with an onset $T_c = 30$ K (i.e. on the T_c plateau) as confirmed in LSCO crystal samples (Fig. 1.14). The relevant results are detailed by developing the idea of a stabilized exciton phase formed during a Mott–Hubbard transition. An earlier theoretical calculation did yield a crystalline arrangement of the doped holes at $x = 1/16$ for a reasonable choice of parameters [63]. The energy gain for charge ordered *d*-wave resonating valence bond (RVB) states in doped cuprates was estimated within a generalized *t-J* model [64]. While the kinetic energy favors a uniform charge distribution, the long-range Coulomb repulsion tends to spatially modulate the charge density in favor of charge ordered RVB states. On the other hand, hole-doping dependence of in-plane resistivity was carefully examined on a series of high-quality $La_{2-x}Sr_xCuO_4$ single crystals [65]. A tendency towards charge ordering at particular doping fractions of 1/16, 3/32, 1/8 and 3/16 was reported (Fig. 1.17), consistent with the *SO*(5) theory prediction of two-dimensional checkerboard ordering of the Cooper pairs at magic rational doping fractions $(2m + 1)/2^n$ (m and n are integers) [66–68].

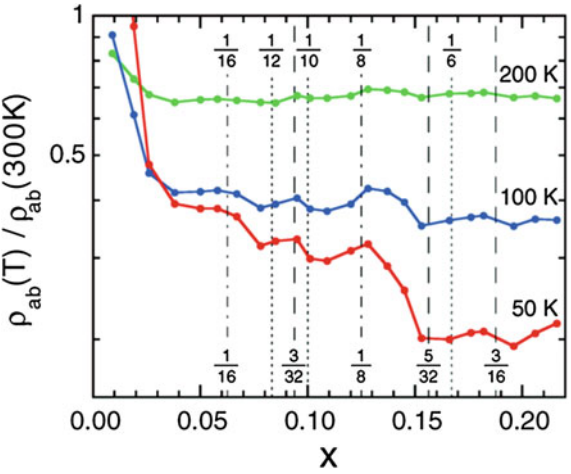

Fig. 1.17 x dependence of $\rho_{ab}(T)/\rho_{ab}$ (300 K) at T = 200, 100 and 50 K for $La_{2-x}Sr_xCuO_4$ single crystals. The hole motion tends to be hindered at low temperature at $x \approx 0.06$, 0.09, 0.13 and 0.18. The magic doping fractions expected for the checkerboard order and the 1D stripes are shown by dashed and dotted lines, respectively; dash-dotted lines show the fractions both models predict. From [65]

1.6 Concluding Remarks

Among the cuprate superconductors, the K_2NiF_4-type $La_{2-x}M_xCuO_4$ is important for the study on cuprate physics in many respects. It exhibits a wide charge doping range showing remarkable and informative doping dependent anomalies, while having fewer components and a simple layered structure containing single CuO_2 planes. Moreover, the TSFZ crystal growth of the substituted $La_{2-x}M_xCuO_4$ has turned out to be very successful and fruitful. Large and high-quality single crystal samples with desired and uniform substitutions have been produced to meet the demand in various specific experimental measurements on intrinsic, anisotropic electronic properties. That has greatly promoted the investigation and understanding of the underlying physics of cuprates. In the aspect of the growth technique, the application of semiconductor laser as the heating source is a new and important development in TSFZ technique, which is promising to make it more powerful to prepare incongruent single crystals difficult for conventional growth methods.

It should be noted that, on one hand, the substitution of dopant M^{2+} for host La^{3+} in La_2CuO_4 induces hole carriers in the CuO_2 planes eventually leading to the superconductivity; on the other hand, it also modifies more or less the crystal lattice of La_2CuO_4, because the dopant, as an introduced "impurity", has a different atomic size and chemical valence compared to that of La^{3+}. Both have significant influences on the electronic properties. In La_2CuO_4 structure, the La^{3+} sites with nine coordinated oxygen anions easily accommodate Sr^{2+} cations having an ionic radius (1.45 Å, by Shannon and Prewitt [69, 70, 71]) properly bigger than La^{3+} (1.356 Å) [72].

The tilt axis of the CuO_6 octahedra is kept diagonal (LTO) to the Cu–O–Cu square lattice and the buckling of CuO_2 planes is reduced with strontium substitution in the under-doping regime, where the robust intrinsic superconducting phases noticeably develop in the vicinity of the magic hole fractions ($La_{2-x}Sr_xCuO_4$). But it is neither the case for the replacement of La^{3+} by Ca^{2+} (1.32 Å) which is too smaller in size, resulting in its low solubility in La_2CuO_4, nor for Ba^{2+} (1.61 Å) which is too bigger, leading to the alternating tilt axes parallel (LTT) to the Cu–O bonds, which pins the charge and spin stripe order thus strongly suppresses the superconductivity (the 1/8 anomaly in $La_{2-x}Ba_xCuO_4$). These have made the cuprate physics more complicated.

Soon after the discovery of high-T_c superconductivity derived from La_2CuO_4 through hole doping, Anderson [73] pointed out that a common, unique feature of the doped cuprates is the proximity to a peculiar insulating magnetic phase with low dimensionality and the underlying physics is hence predominantly electronic and magnetic. This is particularly true in view of anomalous phenomena in cuprates fundamentally different from conventional metal physics, especially the one- or two-dimensional charge and spin physics correlated to the crystal chemistry predominating in $La_{2-x}Ba_xCuO_4$ and $La_{2-x}Sr_xCuO_4$, respectively. With the advances in crystal growth and probing techniques, fruitful results with important implications for the high-T_c superconductivity have been obtained and concepts proposed for attempts to understand them in the past three decades. However, to fully characterize the anomalous phenomena present in the high-T_c superconductors has been a challenging task. A systematic understanding of the microscopic high-T_c mechanism is still lacking up to date.

References

1. J.G. Bednorz, K.A. Muller, Z. Phys. B Condens. Matter **64**, 189 (1986)
2. M. Hucker, M. von Zimmermann, G.D. Gu, Z.J. Xu, J.S. Wen, G.Y. Xu, H.J. Kang, A. Zheludev, J.M. Tranquada, Phys. Rev. B **83**, 104506 (2011)
3. A. Wattiaux, J.C. Park, J.C. Grenier, M. Pouchard, C. R. Acad. Sci. Ser II **310**, 1047 (1990)
4. J.C. Grenier, A. Wattiaux, N. Lagueyte, J.C. Park, E. Marquestaut, J. Etourneau, M. Pouchard, Physica C **173**, 139 (1991)
5. J.E. Schirber, B. Morosin, R.M. Merrill, P.F. Hlava, E.L. Venturini, J.F. Kwak, P.J. Nigrey, R.J. Baughman, D.S. Ginley, Phys. C **152**, 121 (1988)
6. J.D. Jorgensen, B. Dabrowski, S.Y. Pei, D.G. Hinks, L. Soderholm, B. Morosin, J.E. Schirber, E.L. Venturini, D.S. Ginley, Phys. Rev. B **38**, 11337 (1988)
7. J. Orenstein, A.J. Millis, Science **288**, 468 (2000)
8. R.J. Birgeneau, C. Stock, J.M. Tranquada, K. Yamada, J. Phys. Soc. Jpn. **75**, 111003 (2006)
9. J.D. Axe, A.H. Moudden, D. Hohlwein, D.E. Cox, K.M. Mohanty, A.R. Moodenbaugh, Y. Xu, Phys. Rev. Lett. **62**, 2751 (1989)
10. Y. Maeno, A. Odagawa, N. Kakehi, T. Suzuki, T. Fujita, Phys. C **173**, 322 (1991)
11. J.M. Tranquada, B.J. Sternlieb, J.D. Axe, Y. Nakamura, S. Uchida, Nature **375**, 561 (1995)
12. M.K. Crawford, R.L. Harlow, E.M. McCarron, W.E. Farneth, J.D. Axe, H. Chou, Q. Huang, Phys. Rev. B **44**, 7749 (1991)
13. M. Ma, D. Yuan, Y. Wu, H. Zhou, X. Dong, F. Zhou, Supercond. Sci. Technol. **27**, 122001 (2014)

14. S.M. Koohpayeh, D. Fort, J.S. Abell, Prog. Cryst. Growth Charact. **54**, 121 (2008)
15. H. Kojima, I. Tanaka, Jpn. J. Appl. Phys. Ser. **7**, 76 (1992)
16. I. Shindo, J. Cryst. Growth **50**, 839 (1980)
17. I. Tanaka, J. Yamamoto, Y. Mori, H. Tanabe, M.K.R. Khan, H. Kojima, Phys. C **225**, 185 (1994)
18. H. Kojima, J. Yamamoto, Y. Mori, M.K.R. Khan, H. Tanabe, I. Tanaka, Phys. C **293**, 14 (1997)
19. C.-H. Lee, N. Kaneko, S. Hosoya, K. Kurahashi, S. Wakimoto, K. Yamada, Y. Endoh, Supercond. Sci. Technol. **11**, 891 (1998)
20. S. Kimura, I. Shindo, J. Cryst. Growth **41**, 192 (1977)
21. I. Shindo, N. Li, K. Kitamura, S. Kimura, J. Cryst. Growth **46**, 307 (1979)
22. I. Shindo, N. Kimizuka, S. Kimura, Mater. Res. Bull. **11**, 637 (1976)
23. F. Zhou, W.X. Ti, J.W. Xiong, Z.X. Zhao, X.L. Dong, P.H. Hor, Z.H. Zhang, W.K. Chu, Supercond. Sci. Tech. **16**, L7 (2003)
24. X.L. Shen, Z.C. Li, C.X. Shen, W. Lu, X.L. Dong, F. Zhou, Z.X. Zhao, Chin. Phys. B **18**, 2893 (2009)
25. C. Marin, T. Charvolin, D. Braithwaite, R. Calemczuk, Phys. C **320**, 197 (1999)
26. S. Hosoya, C.H. Lee, S. Wakimoto, K. Yamada, Y. Endoh, Phys. C **235–240**(Part 1), 547 (1994)
27. A. Maljuk, S. Watauchi, I. Tanaka, H. Kojima, J. Cryst. Growth **212**, 138 (2000)
28. Y. Hidaka, Y. Enomoto, M. Suzuki, M. Oda, T. Murakami, J. Cryst. Growth **85**, 581 (1987)
29. I. Tanaka, H. Kojima, Nature **337**, 21 (1989)
30. I. Tanaka, K. Yamane, H. Kojima, J. Cryst. Growth **96**, 711 (1989)
31. T.F.S. Hosoya, T. Kajitani, K. Hiraga, K. Oh-Ishi, Y. Syono, K. Yamada, Y. Endoh, T. Takahashi, H. Katayama-Yoshida, Jpn. J. Appl. Phys. Ser. **7**, 81 (1992)
32. K. Oka, M.J.V. Menken, Z. Tarnawski, A.A. Menovsky, A.M. Moe, T.S. Han, H. Unoki, T. Ito, Y. Ohashi, J. Cryst. Growth **137**, 479 (1994)
33. T. Ito, K. Oka, Phys. C **231**, 305 (1994)
34. A.M. Balbashev, D.A. Shulyatev, G.K. Panova, M.N. Khlopkin, N.A. Chernoplekov, A.A. Shikov, A.V. Suetin, Phys. C **256**, 371 (1996)
35. A.K.M.A. Islam (Ed.), in *High-Tc Superconductors: Proceedings of the 12th Anniversary HTS Workshop.* Rajshahi (1998)
36. S. Komiya, Y. Ando, X.F. Sun, A.N. Lavrov, Phys. Rev. B **65**, 214535 (2002)
37. M. Fujita, K. Yamada, H. Hiraka, P. Gehring, S. Lee, S. Wakimoto, G. Shirane, Phys. Rev. B **65**, 064505 (2002)
38. J. Yu, Y. Yanagida, H. Takashima, Y. Inaguma, M. Itoh, T. Nakamura, Phys. C **209**, 442 (1993)
39. T. Adachi, T. Noji, Y. Koike, Phys. Rev. B **64**, 144524 (2001)
40. M. Fujita, H. Goka, K. Yamada, J.M. Tranquada, L.P. Regnault, Phys. Rev. B **70**, 104517 (2004)
41. T. Valla, A.V. Fedorov, J. Lee, J.C. Davis, G.D. Gu, Science **314**, 1914 (2006)
42. M.K.R. Khan, Y. Mori, I. Tanaka, H. Kojima, Phys. C **262**, 202 (1996)
43. M.A.R. Sarker, S. Watauchi, M. Nagao, T. Watanabe, I. Shindo, I. Tanaka, Phys. C **472**, 87 (2012)
44. T. Ito, T. Ushiyama, Y. Yanagisawa, Y. Tomioka, I. Shindo, A. Yanase, J. Cryst. Growth **363**, 264 (2013)
45. T. Ito, T. Ushiyama, Y. Yanagisawa, R. Kumai, Y. Tomioka, Cryst. Growth Des. **11**, 5139 (2011)
46. F.C. Chou, N.R. Belk, M.A. Kastner, R.J. Birgeneau, A. Aharony, Phys. Rev. Lett. **75**, 2204 (1995)
47. S. Wakimoto, G. Shirane, Y. Endoh, K. Hirota, S. Ueki, K. Yamada, R.J. Birgeneau, M.A. Kastner, Y.S. Lee, P.M. Gehring, S.H. Lee, Phys. Rev. B **60**, R769 (1999)
48. J.B. Torrance, Y. Tokura, A.I. Nazzal, A. Bezinge, T.C. Huang, S.S.P. Parkin, Phys. Rev. Lett. **61**, 1127 (1988)

49. K. Sreedhar, P. Ganguly, Phys. Rev. B **41**, 371 (1990)
50. T. Nagano, Y. Tomioka, Y. Nakayama, K. Kishio, K. Kitazawa, Phys. Rev. B **48**, 9689 (1993)
51. P.G. Radaelli, D.G. Hinks, A.W. Mitchell, B.A. Hunter, J.L. Wagner, B. Dabrowski, K.G. Vandervoort, H.K. Viswanathan, J.D. Jorgensen, Phys. Rev. B **49**, 4163 (1994)
52. F. Zhou, P.H. Hor, X.L. Dong, W.X. Ti, J.W. Xiong, Z.X. Zhao, Phys. C **408–410**, 430 (2004)
53. F. Zhou, P.H. Hor, X.L. Dong, Z.X. Zhao, Sci. Technol. Adv. Mater. **6**, 873 (2005)
54. J.M. Tranquada, J.D. Axe, N. Ichikawa, Y. Nakamura, S. Uchida, B. Nachumi, Phys. Rev. B **54**, 7489 (1996)
55. Y.H. Kim, P.H. Hor, X.L. Dong, F. Zhou, Z.X. Zhao, Y.S. Song, W.X. Ti, J. Phys.: Condens. Matter **15**, 8485 (2003)
56. Y.H. Kim, P.H. Hor, X.L. Dong, F. Zhou, Z.X. Zhao, Z. Wu, J.W. Xiong, Phys. Rev. B **71**, 092508 (2005)
57. X.L. Dong, P.H. Hor, F. Zhou, Z.X. Zhao, Solid State Commun. **145**, 173 (2008)
58. X.L. Dong, P.H. Hor, F. Zhou, Z.X. Zhao, Solid State Commun. **152**, 1513 (2012)
59. D. Mihailovic, Phys. Rev. Lett. **94**, 207001 (2005)
60. X.J. Zhou, T. Yoshida, D.H. Lee, W.L. Yang, V. Brouet, F. Zhou, W.X. Ti, J.W. Xiong, Z.X. Zhao, T. Sasagawa, T. Kakeshita, H. Eisaki, S. Uchida, A. Fujimori, Z. Hussain, Z.X. Shen, Phys. Rev. Lett. **92**, 187001 (2004)
61. X.J. Zhou, T. Yoshida, A. Lanzara, P.V. Bogdanov, S.A. Kellar, K.M. Shen, W.L. Yang, F. Ronning, T. Sasagawa, T. Kakeshita, T. Noda, H. Eisaki, S. Uchida, C.T. Lin, F. Zhou, J. W. Xiong, W.X. Ti, Z.X. Zhao, A. Fujimori, Z. Hussain, Z.X. Shen, Nature **423**, 398 (2003)
62. M. Pouchard, J.P. Doumerc, A. Villesuzanne, New J. Chem. **36**, 796 (2012)
63. H.C. Fu, J.C. Davis, D.-H. Lee, arXiv:cond-mat/0403001v2 (2004)
64. H.X. Huang, Y.Q. Li, F.C. Zhang, Phys. Rev. B **71**, 184514 (2005). See also P.W. Anderson, arXiv:cond-mat/0406038v1 (2004), where a two-dimensional crystal of hole pairs embedded in a sea of a d-wave RVB states was proposed, and the energy gain furnished by the long-range Coulomb interaction, something like the Madelung energy of the charge distribution of the "liquid crystal", was suggested
65. S. Komiya, H.-D. Chen, S.-C. Zhang, Y. Ando, Phys. Rev. Lett. **94**, 207004 (2005)
66. H.-D. Chen, J.-P. Hu, S. Capponi, E. Arrigoni, S.-C. Zhang, Phys. Rev. Lett. **89**, 137004 (2002)
67. H.-D. Chen, O. Vafek, A. Yazdani, S.-C. Zhang, Phys. Rev. Lett. **93**, 187002 (2004)
68. H.-D. Chen, S. Capponi, F. Alet, S.-C. Zhang, Phys. Rev. B **70**, 024516 (2004)
69. R.D. Shannon, C.T. Prewitt, Acta Cryst. B **25**, 925 (1969)
70. R.D. Shannon, C.T. Prewitt, Acta Cryst. B **26**, 1046 (1970)
71. R.D. Shannon, Acta Cryst. A **32**, 751 (1976)
72. M.J. Rosseinsky, K. Prassides, P. Day, J. Mater. Chem. **1**, 597 (1991)
73. P.W. Anderson, Science **235**, 1196 (1987)

http://www.springer.com/978-3-319-31546-1

Growth and Characterization of Bulk Superconductor Material

Chen, D.; Lin, C.; Maljuk, A.; Zhou, F.

2016, XI, 196 p. 136 illus., 58 illus. in color., Hardcover
ISBN: 978-3-319-31546-1